PHYSICS

Probing quantum coherence in single-atom electron spin resonance

Philip Willke,[1,2,3,4] William Paul,[2] Fabian D. Natterer,[2,5] Kai Yang,[2] Yujeong Bae,[1,2,3] Taeyoung Choi,[1,3] Joaquin Fernández-Rossier,[6]* Andreas J. Heinrich,[1,3]† Christoper P. Lutz[2]†

Spin resonance of individual spin centers allows applications ranging from quantum information technology to atomic-scale magnetometry. To protect the quantum properties of a spin, control over its local environment, including energy relaxation and decoherence processes, is crucial. However, in most existing architectures, the environment remains fixed by the crystal structure and electrical contacts. Recently, spin-polarized scanning tunneling microscopy (STM), in combination with electron spin resonance (ESR), allowed the study of single adatoms and inter-atomic coupling with an unprecedented combination of spatial and energy resolution. We elucidate and control the interplay of an Fe single spin with its atomic-scale environment by precisely tuning the phase coherence time T_2 using the STM tip as a variable electrode. We find that the decoherence rate is the sum of two main contributions. The first scales linearly with tunnel current and shows that, on average, every tunneling electron causes one dephasing event. The second, effective even without current, arises from thermally activated spin-flip processes of tip spins. Understanding these interactions allows us to maximize T_2 and improve the energy resolution. It also allows us to maximize the amplitude of the ESR signal, which supports measurements even at elevated temperatures as high as 4 K. Thus, ESR-STM allows control of quantum coherence in individual, electrically accessible spins.

INTRODUCTION

Coherent control and detection of individual electron and nuclear spins have been studied intensively with the aim to determine molecular and electronic structures (1, 2), to resolve magnetic interactions between spins (3–8), and to serve as quantum bits (qubits) for quantum information processing (9). Electrical control of single qubits was realized for quantum dots (10), phosphorus donors in silicon (11), and molecular magnets (12). Crucial properties of a quantum spin are the phase coherence time T_2 and the energy relaxation time T_1, which are constrained by the interaction with the environment. Whereas T_1 describes how long a spin remains in a given energy eigenstate, T_2 characterizes the time before information about the quantum phase of the spin is lost. Identifying and disentangling sources of scattering and decoherence therefore become essential for quantum devices (13). Most existing techniques operate with a fixed device geometry, and the atomic-scale environment is often neither controlled nor known locally. Scanning probe methods provide routine control at the atomic scale and were used to fabricate, characterize, and read out spin structures (14–20). The influence of the environment on T_1 has been intensively studied using scanning tunneling microscopy (STM) for single adatoms (7, 16, 17, 21–23), molecules (24), dopants (25, 26), and nanostructures (27–34). In contrast, T_2 is largely unexplored except for theoretical studies (35–42). Coherence times only recently became accessible in STM by using a radio frequency (RF) electric field to drive electron spin resonance (ESR) of individual atoms (43, 44).

[1]Center for Quantum Nanoscience, Institute for Basic Science, Seoul 03760, Republic of Korea. [2]IBM Almaden Research Center, San Jose, CA 95120, USA. [3]Department of Physics, Ewha Womans University, Seoul 03760, Republic of Korea. [4]IV. Physical Institute, University of Göttingen, Friedrich-Hund-Platz 1, 37077 Göttingen, Germany. [5]Institute of Physics, École Polytechnique Fédérale de Lausanne, CH-1015 Lausanne, Switzerland. [6]QuantaLab, International Iberian Nanotechnology Laboratory, Avenida Mestre José Veiga, 4715-310 Braga, Portugal.
*On leave from Departamento de Física Aplicada, Universidad de Alicante, San Vicente del Raspeig 03690, Spain.
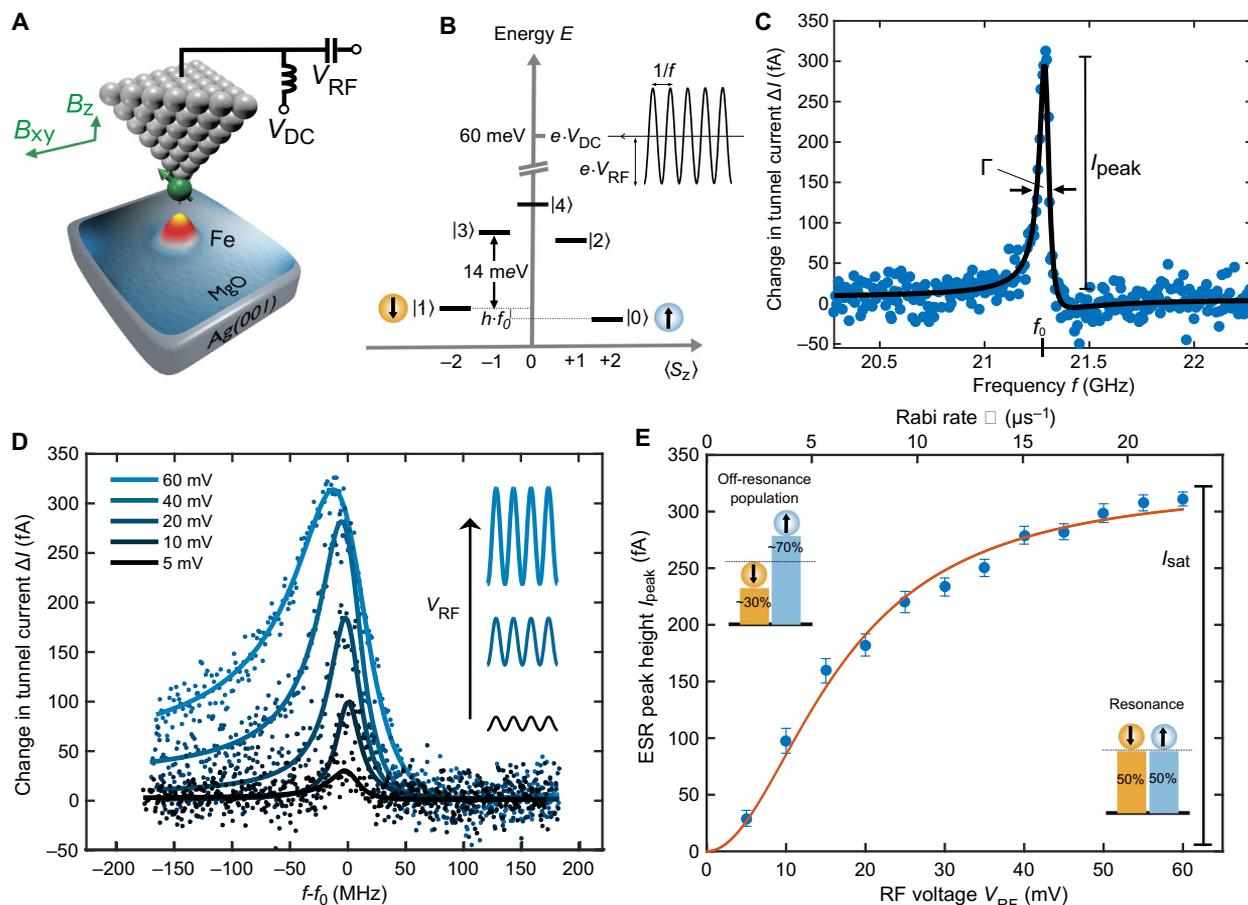†Corresponding author. Email: heinrich.andreas@qns.science (A.J.H.); cplutz@us.ibm.com (C.P.L.)

Here, we use ESR-STM to demonstrate control over the interaction of a single Fe atom spin with its environment by selecting the tip position and the tunneling parameters. We find that nearly every tunneling electron leads to a loss in phase coherence. Consequently, lowering the tunnel current improves the phase coherence time, as required for quantum logic operations and for maximizing the energy resolution. Despite the current-induced loss of phase coherence, we demonstrate that the largest spin resonance signal can be obtained by using large tunnel currents. This greatly assists single-atom spin resonance as a quantum sensor, for example, to measure single atoms' magnetic moments as demonstrated recently (6–8). Moreover, it readily allows ESR at higher temperatures (up to 4 K) and relatively small magnetic fields—conditions that are available in many low-temperature STM setups. Besides the great improvement in signal, studying spin resonance in a broad range of tunnel currents and temperatures allows us to investigate, control, and distinguish decoherence mechanisms on a single-atom level.

RESULTS

The experimental setup of our ESR-STM is shown in Fig. 1A. We use single, isolated iron (Fe) atoms located on two atomic layers of MgO on an Ag(001) substrate (see also section S1) (45). To realize ESR, we applied an RF voltage V_{RF} to the tunneling junction in addition to the conventional DC bias voltage V_{DC}. The RF voltage induces coherent transitions between the Zeeman-split low-energy states $|0\rangle$ and $|1\rangle$ at the resonance frequency f_0 (Fig. 1B) (43, 44). Magnetoresistive sensing of the steady-state spin population is achieved by using a magnetic tip to give different conductances for the two low-energy spin states. Magnetic tips were prepared by picking up Fe atoms (typically one to five) from the surface until ESR signal was obtained. We use DC voltages of up to $V_{DC} = 60\,\text{mV}$, exceeding the spin excitation thresholds (Fig. 1B), and apply V_{RF} amplitudes that result in larger Rabi flop rates than previously observed (43), because this yields larger ESR signals. This is caused by additional spin-torque initialization of the spin state,

Fig. 1. High-signal ESR in a scanning tunneling microscope. (**A**) Experimental setup showing a colorized STM topography of a single Fe atom on MgO/Ag(001). For ESR, the applied voltage consists of the conventional DC bias voltage V_{DC} and an additional RF voltage V_{RF}. The green tip atom indicates the presence of a magnetic tip apex. (**B**) Energy-level diagram of the lowest five energy levels of the Fe atom. The out-of-plane component B_z of the magnetic field splits the lowest two levels, $|0\rangle$ and $|1\rangle$, by $f_0 \approx 21$ GHz (87 μeV). (**C**) ESR spectrum (change in tunnel current ΔI as a function of frequency f) for the atom shown in (A). Solid line is a fit to an asymmetric Lorentzian [$\Delta I = I_{peak}/(1 + \left[\frac{f-f_0}{\Gamma/2}\right]^2)$; see section S2.1 for peak asymmetry caused by the contribution of homodyne detection]. Resonance frequency f_0, peak height I_{peak}, and linewidth Γ are indicated ($I = 20$ pA, $V_{DC} = 60$ mV, $V_{RF} = 30$ mV zero to peak). (**D**) ESR peaks for different V_{RF} ($I = 11$ pA, $V_{DC} = 60$ mV). (**E**) I_{peak} (V_{RF}) for the data sets shown in (D). The peak height is saturating at I_{sat}, because the on-resonance population of states $|0\rangle$ and $|1\rangle$ is driven into nearly equal occupation (illustrated by bar graphs). The scale for the Rabi flop rate Ω is additionally shown.

which actively drives the spin population toward the ground state (16). Figure 1C shows a typical ESR peak: The tunnel current changes by ΔI because of a change in the state populations. I_{peak} is the amplitude of the peak, which can be described by the solution of the Bloch equations of a two-level system (2, 38, 43)

$$I_{peak} = I_{sat} \cdot \frac{\Omega^2 T_1 T_2}{\Omega^2 T_1 T_2 + 1} \qquad (1)$$

where the Rabi flop rate Ω is proportional to V_{RF}. Consequently, the ESR spectra show an increase in I_{peak} (Fig. 1D) for increasing V_{RF}, which reflects the growing deviation from the off-resonance population. In the low-current limit, this is equal to the thermal population. Ultimately, the RF voltage is strong enough to equalize the population of states $|0\rangle$ and $|1\rangle$, and the saturation current I_{sat} is reached (Fig. 1E). Details and additional information about the ESR peak analysis, as well as spin-torque initialization, are provided in section S2.

Tunnel current–induced decoherence

Following Eq. 1, the evolution of the peak height and linewidth as a function of V_{RF} and tunnel current I reveals information on both T_1 and T_2. In general, both increase with greater decoupling from the environment (2, 13, 38), which, in the present case, is determined by the interaction with the tip. The STM tip was previously shown to act as an electrode with variable coupling that effectively tunes T_1 (16, 22). Lower I values decrease the rate with which a tunneling electron is transmitted from the tip, scatters with the Fe spin, and is transmitted into the silver substrate (or opposite, depending on the polarity of the DC voltage). In Fig. 2A, we plot the linewidth Γ for constant V_{RF} for different I values, demonstrating a narrowing of the peak at lower tunnel currents. We use the relation $\Gamma = \frac{1}{\pi T_2}\sqrt{1 + T_1 T_2 \Omega^2}$ corresponding to the ESR peak of Eq. 1 (2, 38, 43) to extract the current-dependent T_2 from the slope of the curves in Fig. 2B. Note that the influence of inhomogeneous broadening due to slowly fluctuating fields is avoided in this means of determining T_2. These fluctuations are here caused by slow ~1 pm shaking of the tip that leads to a change in f_0 by the tip magnetic field (43). Figure 2C shows that T_2 increases rapidly
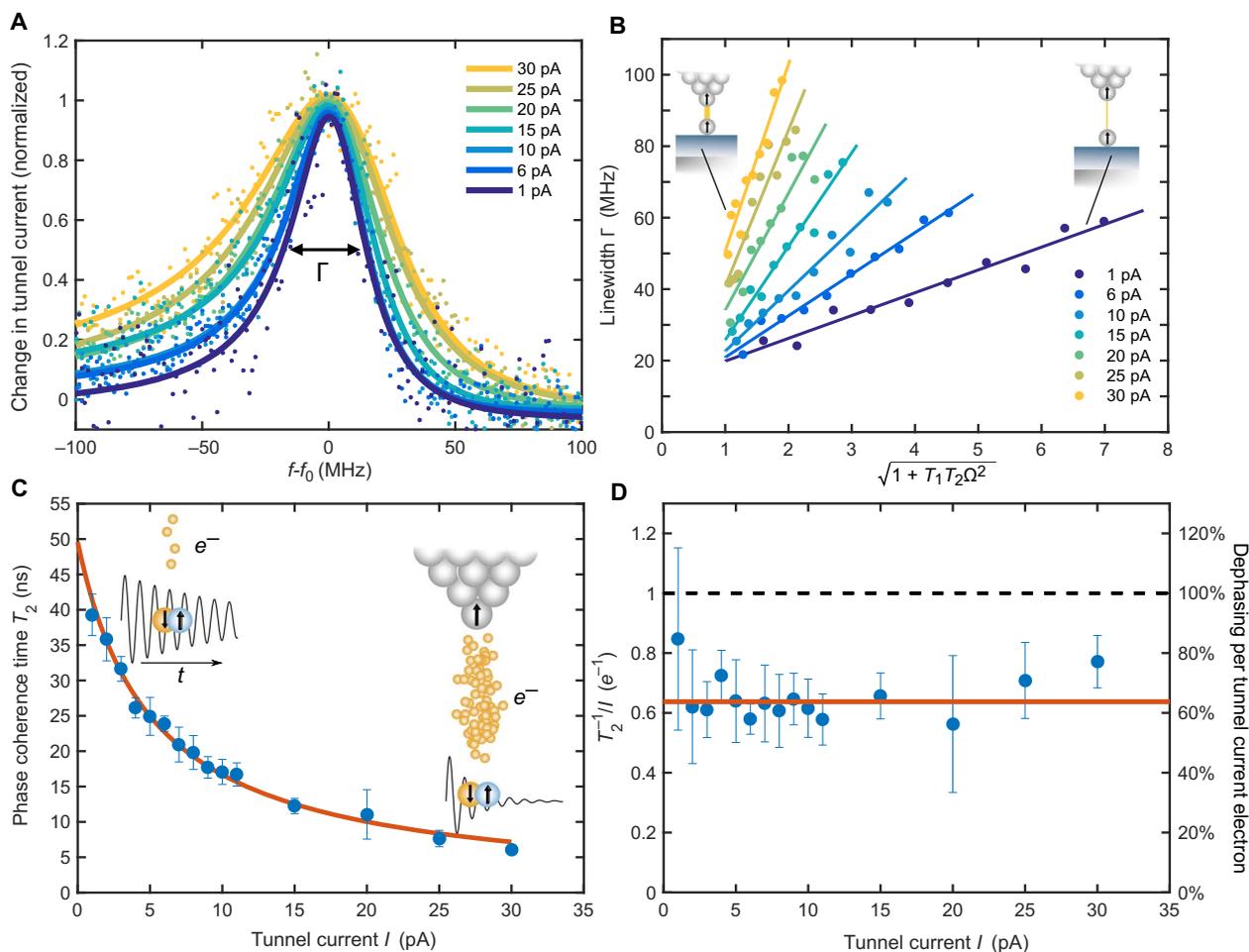
Fig. 2. Phase coherence time measurements. (**A**) ESR peaks for different tunnel currents (color-coded), normalized and shifted vertically for visibility. The RF voltage is kept at $V_{RF} = 30\,\text{mV}$. (**B**) ESR linewidth Γ as a function of the adjusted drive amplitude $\sqrt{1 + \Omega^2 T_1 T_2}$ for different tunnel currents $I = 1$ to 30 pA (color-coded). The resulting slope equals $(\pi T_2)^{-1}$. (The proportionality relating $\Omega^2 T_1 T_2$ and V_{RF} was first determined independently for each I by fitting the peak height as in Fig. 1E; see sections S2.2 and S4.1.) (**C**) Phase coherence times $T_2(I)$ deduced from (B). The sketches emphasize the gain in phase coherence for diminishing tunnel current. We here find $T_2 \propto I^{-1}$ (or $T_2^{-1} \propto I$). (**D**) Dephasing rate per tunneling electron T_2^{-1}/I derived from (C) [offset in $1/T_2$ at $I = 0$ has been subtracted]. The dark orange ($0.64\,e^{-1}$) is the slope of the linear fit to the data in (C). The black dashed line indicates the case where every tunneling electron dephases the Fe atom's spin.

with decreasing I, reflecting the decreasing rate of decoherence T_2^{-1}. We find here an inverse proportional behavior $T_2^{-1} \propto I$, suggesting that each tunneling electron interacting with the Fe spin leads to a loss in phase information as sketched in Fig. 2C (additional information on the effect of tip shaking and further T_2 measurements are given in section S3). Figure 2D shows the average probability $P_{T_2} = e T_2^{-1}/I$ of an electron to destroy the phase information of the spin system. We find that most of the tunneling electrons $[P_{T_2} = (64 \pm 7)\%]$ result in dephasing. In contrast, despite the use of relatively high voltages (greater than the inelastic excitation voltage), energy relaxation between the $|0\rangle$ and $|1\rangle$ states (T_1 processes) occurs at a rate of only $P_{T_1} = (0.5 \pm 0.1)\%$ per tunneling electron (see section S4). Therefore, T_1^{-1} only contributes negligibly to T_2^{-1}. Moreover, no significant dependence of T_2 on V_{DC} was found (see inset in Fig. 3A), making the decoherence time independent of the energy of the tunneling electrons.

The above measurements show how efficiently the Fe spin interacts with the tunneling electrons. Because we depend on the tunneling current for readout, maintaining phase coherence is challenging. Nevertheless, by using a low tunneling current to maximize T_2, we improve the resolution in magnetometry experiments (6, 38) through a decreased linewidth.

To model the decoherence process, we consider two tunneling channels: one spin-independent and one spin-dependent. The latter is due to the exchange interaction of the tunneling electrons with the surface spin. Each of these tunneling events adds an extra exchange term to the Zeeman Hamiltonian. This leads to a transient change in resonance frequency and, therefore, to a relative phase shift between the $|0\rangle$ and $|1\rangle$ Fe states. Consequently, the relative phase of the Fe spin is shifted by a fraction of tunneling electrons and performs a random walk causing decoherence (38). Besides this heuristic approach, we also apply the Bloch-Redfield theory to the problem. Both models are able to explain the linear dependence between the current and decoherence rate observed experimentally (see section S5).

Tunnel current–independent decoherence

The rate equation for T_2 scattering can be written as the sum of contributions

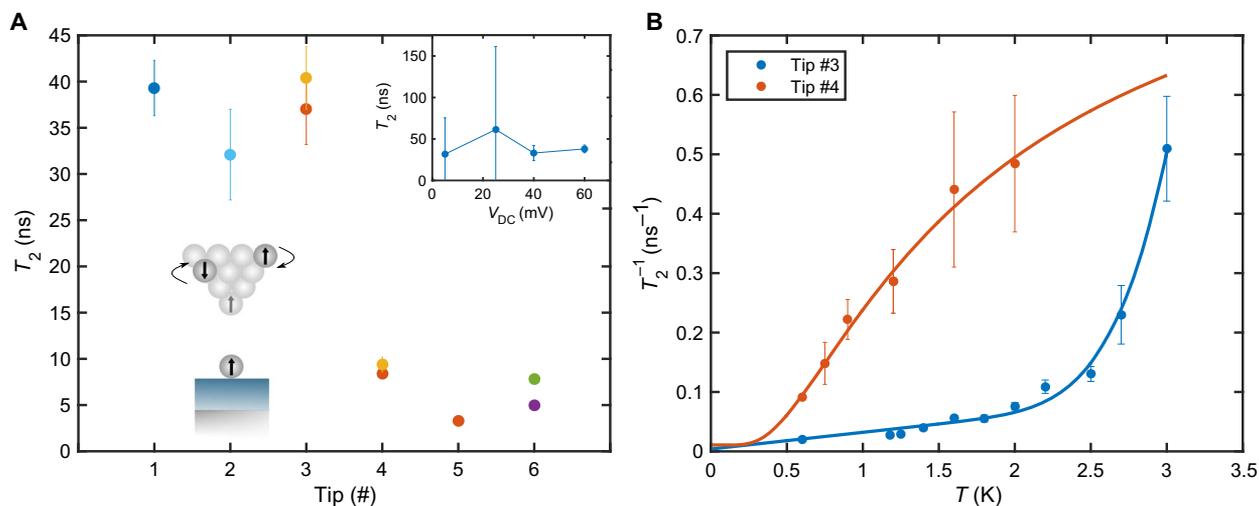$$T_2^{-1} = \frac{P_{T_2}}{e} \cdot I + T_2^{-1}(0) \qquad (2)$$

Fig. 3. Tip, temperature, and bias dependence of T_2. (**A**) T_2 measured for six different spin-polarized STM tips ($I = 1$ to $2\,\mathrm{pA}$, $V_{DC} = 60\,\mathrm{mV}$, $T = 1.2\,\mathrm{K}$). Colors indicate different Fe atoms on the surface. The sketch illustrates the switching of magnetic atoms on the tip, which causes a decrease in T_2 for some tips. Inset shows the independence of T_2 on V_{DC} ($I = 2\,\mathrm{pA}$). (**B**) Decoherence rate T_2^{-1} measured as a function of temperature for two different tips [tips #3 and #4 in (A)] on the same Fe atom ($I = 1\,\mathrm{pA}$, $V_{DC} = 60\,\mathrm{mV}$). Solid lines are fits using the model of eq. S17 (see section S3.3).

Here, $T_2^{-1}(0)$ represents the current-independent decoherence rate. By extrapolating $T_2^{-1}(I)$ to the zero-current limit (Fig. 2C), we obtain $T_2^{-1}(0) = (50 \pm 6\,\mathrm{ns})^{-1}$.

To understand the origin of $T_2^{-1}(0)$, we investigate the tip dependence of T_2. For different magnetic tips, we observe widely varied T_2 times, even for the same Fe atom on the surface (Fig. 3A). In addition, we measured T_2 as a function of temperature T for two different tips (Fig. 3B) for which we find an Arrhenius-type thermal activation process proportional to $\exp(-T_0/T)$, where the characteristic temperature T_0 depends strongly on the tip. We propose that this tip-dependent thermally activated decoherence is induced by spin-flip events occurring within the tip's magnetic atom assembly (see sketch Fig. 3A), similar to decoherence observed in other systems (13, 46). This mechanism predicts that the Fe spin's phase coherence is proportional to the tip's spin-flip time $T_2 \propto T_{1,\mathrm{tip}}$ (13, 46). Therefore, the more rapid decoherence at higher temperature is caused by the higher spin-flip rate of the tip. A similar temperature dependence of T_1 was observed previously for magnetic atom assemblies on a surface (27, 28). (For additional discussion on the temperature dependence of T_2, see section S3.3.) We note that this mechanism relates to scanning probe relaxometry (5, 47–49), where the change in lifetime and phase coherence of a nitrogen vacancy (NV) center is used to determine the properties of magnetic objects scanned in proximity to an NV center using an atomic force microscope.

High-current readout

The current-independent loss of phase coherence impedes the observation of ESR, especially at higher temperatures. Nevertheless, the use of higher tunnel currents in the readout can compensate for the reduction of T_2 by reaching higher peak amplitudes. As shown in Fig. 4A, I_{sat} is linear in I up to the highest tunnel currents used. Here, the slope is determined by the tip spin polarization and the off-resonance population of the Fe atom. This can be derived from a simple two-state model of the conductance of the tunnel junction (see section S2.2). Consequently, the ESR signal can be improved easily by increasing I, provided that V_{RF} is able to drive the spin into saturation (Fig. 1E; see also fig. S4). In Fig. 4B, we demonstrate that despite the decrease in T_2, spin resonance is still readily observed at higher temperatures by using high

readout currents. We found that I_{peak} at $T = 4\,\mathrm{K}$ is reduced to 10 to 40% of the value measured at 1.2 K (Fig. 4B, inset). This reduction is caused by the lower off-resonance polarization (difference in population of states $|0\rangle$ and $|1\rangle$) of the Fe spin at higher temperatures. Moreover, T_2 decreases at higher temperatures as shown above, and similar observations were made for T_1 elsewhere (22). We speculate that the different evolutions with temperature of different data sets in the inset are a consequence of a temperature dependence of the tip spin polarization, which is expected to be unique to each tip (for additional information and discussion on the temperature dependence of the ESR peak, see section S6).

DISCUSSION

Larger tunneling currents allow significant improvement in the ESR signal at the price of an increased linewidth. The demonstration of ESR measurements at 4 K should make ESR-STM and quantum sensing (6, 7) possible in many existing STM systems operating at liquid helium temperature. The ability to use this technique for a broad range of tunnel currents and temperatures allows us to investigate, control, and distinguish decoherence mechanisms on a single-atom level, a crucial requirement for quantum information devices. The strong interaction with the tunneling electrons applies, in general, to any architecture using magnetoresistance for electrical readout, and our results will allow improvement of quantum coherence in single-atom spins. Currently, T_2 is still lower than the Rabi flop time π/Ω, which effectively prohibits coherent manipulations of the spin. Possible routes to increase T_2 include moving the tip laterally away from the atom (47–49), remote sensing (6, 30), and suppression of inelastic tunneling channels (50). In addition, thicker layers of MgO and lower temperatures will suppress dephasing by substrate electrons. Lower temperatures will also decrease spin-flip transitions in the tip. Moreover, we speculate that different atom species (8), molecules, or atom assemblies may show higher T_2 times and Rabi rates because of their different electronic properties. In combination with atom manipulation, ESR-STM will make it possible to design and characterize new nanostructures assembled atom-by-atom that exhibit enhanced phase coherence for quantum applications.
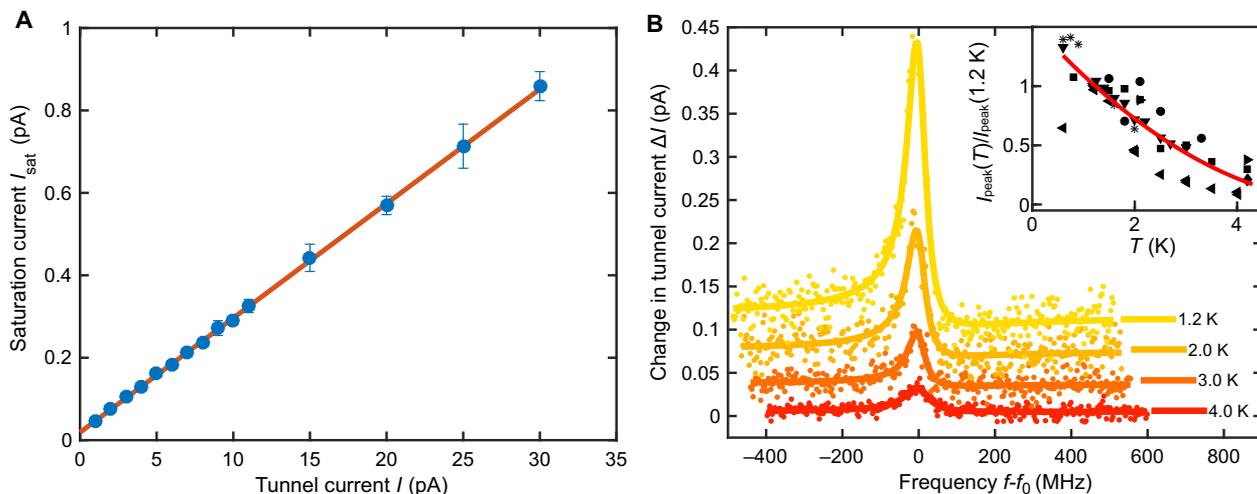
Fig. 4. High-current readout at elevated temperatures. (**A**) Saturation current I_{sat} (see Fig. 1E) as a function of I. Dark orange line is a linear fit to the data points ($V_{DC} = 60$ mV, $T = 1.2$ K). (**B**) ESR spectra given for different temperatures ($I = 20$ pA, $V_{DC} = 60$ mV, $V_{RF} = 30$ mV). Spectra are offset by 40 fA. Inset: Temperature evolution for $I_{peak}(T)$ normalized to $I_{peak}(1.2$ K). Symbols indicate different data sets, each taken at different current and bias voltage set points, with different tips, and on different atoms (see section S6). Red line is used as a guide to the eye.

MATERIALS AND METHODS

Sample preparation

For MgO growth, a Ag(001) single crystal was heated to ~600 K while being exposed to a Mg flux (Knudsen cell) in an oxygen environment of ~10^{-6} mbar. Using a growth rate of ~0.5 monolayers per minute, a MgO coverage of 1.5 monolayers was achieved. Fe atoms were evaporated directly onto the cold sample (<10 K) from a piece of pure metal using e-beam evaporation. Within the scope of this work, all experiments were conducted on two layers of MgO as determined by point-contact measurements (*22*). Note that this bilayer thickness had been previously denoted as monolayer MgO (*43*). The STM measurements used an Ir wire as the tip, which was presumably coated with Ag because of indentations into the Ag surface.

Electron spin resonance

Experiments were performed in a homebuilt, ultrahigh vacuum STM system at the IBM Almaden Research Center operating at 1.2 K. We achieved a Zeeman splitting of 87 μeV ≈ 21 GHz for the lowest two energy levels, $|0\rangle$ and $|1\rangle$, of the Fe spin system [the diagram of all five lowest-lying spin states (*45*) is shown in Fig. 1B] by applying a magnetic field of 0.9 T, having an out-of-plane component $B_z \approx 150$ mT (Fe on this surface showed large easy-axis anisotropy in the out-of-plane direction, so only B_z contributed to Zeeman splitting). We improved the ESR signal by using larger V_{RF} and V_{DC} than were used previously (*43*). We found that larger V_{RF} and V_{DC} gave a better ESR signal despite the marked reduction in T_1, resulting from transitions between the $|0\rangle$ and $|1\rangle$ states that were induced via the higher-energy states $|2\rangle$, $|3\rangle$, and $|4\rangle$. Operation at this high V_{DC} also assisted by driving the spin state toward polarization (it "initialized" the spin state, in competition with spin-resonant depolarization) as a result of spin-torque initialization (see section S2.3) (*16*). This spin-torque initialization occurred in addition to polarization by relaxation toward the thermal population of the $|0\rangle$ and $|1\rangle$ states used in previous experiments (*6*, *43*).

SUPPLEMENTARY MATERIALS

Supplementary material for this article is available at http://advances.sciencemag.org/cgi/content/full/4/2/eaaq1543/DC1
section S1. Local environment of the Fe atom
section S2. Additional peak shape analysis
section S3. Supplementary analysis of phase coherence time T_2
section S4. Evaluation of the T_1 time of the Fe spin
section S5. Theoretical treatment of the linear relation between adatom spin decoherence rate and current
section S6. Temperature dependence of the ESR peak height
fig. S1. Large topography of the Fe atom.
fig. S2. Fano factor $q(V_{RF})$ for different I and V_{DC}.
fig. S3. Change in drive Φ with V_{RF} and I.
fig. S4. Obtaining large ESR signals.
fig. S5. Spin-torque initialization.
fig. S6. Bias voltage analysis.
fig. S7. Broadening of the resonant peak induced by tip vibrations.
fig. S8. Additional data for the phase coherence time T_2.
fig. S9. Bias voltage analysis of the T_2 time.
fig. S10. Pump-probe spectroscopy to determine T_1.
fig. S11. Evaluation of spin lifetime T_1.
fig. S12. Temperature dependence of the peak height.
Reference (*51*)

REFERENCES AND NOTES

1. J. Wrachtrup, C. von Borczyskowski, J. Bernard, M. Orritt, R. Brown, Optical detection of magnetic resonance in a single molecule. *Nature* **363**, 244–245 (1993).
2. A. Abragam, B. Bleaney, *Electron Paramagnetic Resonance of Transition Ions* (Oxford Univ. Press, 2012).
3. J. R. Maze, P. L. Stanwix, J. S. Hodges, S. Hong, J. M. Taylor, P. Cappellaro, L. Jiang, M. G. Dutt, E. Togan, A. S. Zibrov, A. Yacoby, R. L. Walsworth, M. D. Lukin, Nanoscale magnetic sensing with an individual electronic spin in diamond. *Nature* **455**, 644–647 (2008).
4. S. Kotler, N. Akerman, N. Navon, Y. Glickman, R. Ozeri, Measurement of the magnetic interaction between two bound electrons of two separate ions. *Nature* **510**, 376–380 (2014).
5. C. L. Degen, F. Reinhard, P. Cappellaro, Quantum sensing. *Rev. Mod. Phys.* **89**, 035002 (2017).
6. T. Choi, W. Paul, S. Rolf-Pissarczyk, A. J. Macdonald, F. D. Natterer, K. Yang, P. Willke, C. P. Lutz, A. J. Heinrich, Atomic-scale sensing of the magnetic dipolar field from single atoms. *Nat. Nanotechnol.* **12**, 420–424 (2017).
7. F. D. Natterer, K. Yang, W. Paul, P. Willke, T. Choi, T. Greber, A. J. Heinrich, C. P. Lutz, Reading and writing single-atom magnets. *Nature* **543**, 226–228 (2017).

8. K. Yang, Y. Bae, W. Paul, F. D. Natterer, P. Willke, J. L. Lado, A. Ferrón, T. Choi, J. Fernández-Rossier, A. J. Heinrich, C. P. Lutz, Engineering the eigenstates of coupled spin-1/2 atoms on a surface. *Phys. Rev. Lett.* **119**, 227206 (2017).

9. D. D. Awschalom, L. C. Bassett, A. S. Dzurak, E. L. Hu, J. R. Petta, Quantum spintronics: Engineering and manipulating atom-like spins in semiconductors. *Science* **339**, 1174–1179 (2013).

10. F. H. L. Koppens, C. Buizert, K. J. Tielrooij, I. T. Vink, K. C. Nowack, T. Meunier, L. P. Kouwenhoven, L. M. K. Vandersypen, Driven coherent oscillations of a single electron spin in a quantum dot. *Nature* **442**, 766–771 (2006).

11. J. J. Pla, K. Y. Tan, J. P. Dehollain, W. H. Lim, J. J. Morton, D. N. Jamieson, A. S. Dzurak, A. Morello, A single-atom electron spin qubit in silicon. *Nature* **489**, 541–545 (2012).

12. S. Thiele, F. Balestro, R. Ballou, S. Klyatskaya, M. Ruben, W. Wernsdorfer, Electrically driven nuclear spin resonance in single-molecule magnets. *Science* **344**, 1135–1138 (2014).

13. A. M. Tyryshkin, S. Tojo, J. J. Morton, H. Riemann, N. V. Abrosimov, P. Becker, H.-J. Pohl, T. Schenkel, M. L. Thewalt, K. M. Itoh, S. A. Lyon, Electron spin coherence exceeding seconds in high-purity silicon. *Nat. Mater.* **11**, 143–147 (2012).

14. D. Rugar, R. Budakian, H. J. Mamin, B. W. Chui, Single spin detection by magnetic resonance force microscopy. *Nature* **430**, 329–332 (2004).

15. R. Wiesendanger, Spin mapping at the nanoscale and atomic scale. *Rev. Mod. Phys.* **81**, 1495–1550 (2009).

16. S. Loth, K. Von Bergmann, M. Ternes, A. F. Otte, C. P. Lutz, A. J. Heinrich, Controlling the state of quantum spins with electric currents. *Nat. Phys.* **6**, 340–344 (2010).

17. S. Loth, M. Etzkorn, C. P. Lutz, D. M. Eigler, A. J. Heinrich, Measurement of fast electron spin relaxation times with atomic resolution. *Science* **329**, 1628–1630 (2010).

18. M. Fuechsle, J. A. Miwa, S. Mahapatra, H. Ryu, S. Lee, O. Warschkow, L. C. Hollenberg, G. Klimeck, M. Y. Simmons, A single-atom transistor. *Nat. Nanotechnol.* **7**, 242–246 (2012).

19. J. Salfi, J. A. Mol, R. Rahman, G. Klimeck, M. Y. Simmons, L. C. L. Hollenberg, S. Rogge, Spatially resolving valley quantum interference of a donor in silicon. *Nat. Mater.* **13**, 605–610 (2014).

20. G. Gramse, A. Kölker, T. Lim, T. J. Stock, H. Solanki, S. R. Schofield, E. Brinciotti, G. Aeppli, F. Kienberger, N. J. Curson, Nondestructive imaging of atomically thin nanostructures buried in silicon. *Sci. Adv.* **3**, e1602586 (2017).

21. I. G. Rau, S. Baumann, S. Rusponi, F. Donati, S. Stepanow, L. Gragnaniello, J. Dreiser, C. Piamonteze, F. Nolting, S. Gangopadhyay, O. R. Albertini, R. M. Macfarlane, C. P. Lutz, B. A. Jones, P. Gambardella, A. J. Heinrich, H. Brune, Reaching the magnetic anisotropy limit of a 3d metal atom. *Science* **344**, 988–992 (2014).

22. W. Paul, K. Yang, S. Baumann, N. Romming, T. Choi, C. P. Lutz, A. J. Heinrich, Control of the millisecond spin lifetime of an electrically probed atom. *Nat. Phys.* **13**, 403–407 (2017).

23. F. Donati, S. Rusponi, S. Stepanow, C. Wäckerlin, A. Singha, L. Persichetti, R. Baltic, K. Diller, F. Patthey, E. Fernandes, J. Dreiser, Ž. Šljivančanin, K. Kummer, C. Nistor, P. Gambardella, H. Brune, Magnetic remanence in single atoms. *Science* **352**, 318–321 (2016).

24. B. W. Heinrich, L. Braun, J. I. Pascual, K. J. Franke, Protection of excited spin states by a superconducting energy gap. *Nat. Phys.* **9**, 765–768 (2013).

25. P. Kloth, M. Wenderoth, From time-resolved atomic-scale imaging of individual donors to their cooperative dynamics. *Sci. Adv.* **3**, e1601552 (2017).

26. M. Rashidi, J. A. Burgess, M. Taucer, R. Achal, J. L. Pitters, S. Loth, R. A. Wolkow, Time-resolved single dopant charge dynamics in silicon. *Nat. Commun.* **7**, 13258 (2016).

27. S. Loth, S. Baumann, C. P. Lutz, D. M. Eigler, A. J. Heinrich, Bistability in atomic-scale antiferromagnets. *Science* **335**, 196–199 (2012).

28. A. A. Khajetoorians, B. Baxevanis, C. Hübner, T. Schlenk, S. Krause, T. O. Wehling, S. Lounis, A. Lichtenstein, D. Pfannkuche, J. Wiebe, R. Wiesendanger, Current-driven spin dynamics of artificially constructed quantum magnets. *Science* **339**, 55–59 (2013).

29. S. Yoshida, Y. Aizawa, Z.-H. Wang, R. Oshima, Y. Mera, E. Matsuyama, H. Oigawa, O. Takeuchi, H. Shigekawa, Probing ultrafast spin dynamics with optical pump–probe scanning tunneling microscopy. *Nat. Nanotechnol.* **9**, 588–593 (2014).

30. S. Yan, D.-J. Choi, J. Burgess, S. Rolf-Pissarczyk, S. Loth, Control of quantum magnets by atomic exchange bias. *Nat. Nanotechnol.* **10**, 40–45 (2015).

31. A. Spinelli, B. Bryant, F. Delgado, J. Fernandez-Rossier, A. F. Otte, Imaging of spin waves in atomically designed nanomagnets. *Nat. Mater.* **13**, 782–785 (2014).

32. S. Krause, A. Sonntag, J. Hermenau, J. Friedlein, R. Wiesendanger, High-frequency magnetization dynamics of individual atomic-scale magnets. *Phys. Rev. B* **93**, 064407 (2016).

33. S. Yan, L. Malavolti, J. A. Burgess, A. Droghetti, A. Rubio, S. Loth, Nonlocally sensing the magnetic states of nanoscale antiferromagnets with an atomic spin sensor. *Sci. Adv.* **3**, e1603137 (2017).

34. J. Hermenau, J. Ibañez-Azpiroz, C. Hübner, A. Sonntag, B. Baxevanis, K. T. Ton, M. Steinbrecher, A. A. Khajetoorians, M. dos Santos Dias, S. Blügel, R. Wiesendanger, S. Lounis, J. Wiebe, A gateway towards non-collinear spin processing using three-atom magnets with strong substrate coupling. *Nat. Commun.* **8**, 642 (2017).

35. F. Delgado, J. Fernández-Rossier, Storage of classical information in quantum spins. *Phys. Rev. Lett.* **108**, 196602 (2012).

36. J.-P. Gauyacq, N. Lorente, Decoherence-governed magnetic-moment dynamics of supported atomic objects. *J. Phys. Condens. Matter* **27**, 455301 (2015).

37. A. M. Shakirov, Y. E. Shchadilova, A. N. Rubtsov, P. Ribeiro, Role of coherence in transport through engineered atomic spin devices. *Phys. Rev. B* **94**, 224425 (2016).

38. F. Delgado, J. Fernández-Rossier, Spin decoherence of magnetic atoms on surfaces. *Prog. Surf. Sci.* **92**, 40–82 (2017).

39. F. Delgado, J. Fernández-Rossier, RKKY oscillations in the spin relaxation rates of atomic-scale nanomagnets. *Phys. Rev. B* **95**, 075413 (2017).

40. A. M. Shakirov, A. N. Rubtsov, A. I. Lichtenstein, P. Ribeiro, Relaxation and decoherence of qubits encoded in collective states of engineered magnetic structures. *Phys. Rev. B* **96**, 094410 (2017).

41. J. Ibañez-Azpiroz, M. dos Santos Dias, S. Blügel, S. Lounis, Longitudinal and transverse spin relaxation times of magnetic single adatoms: An ab initio analysis. *Phys. Rev. B* **96**, 144410 (2017).

42. J. L. Lado, A. Ferrón, J. Fernández-Rossier, Exchange mechanism for electron paramagnetic resonance of individual adatoms. *Phys. Rev. B* **96**, 205420 (2017).

43. S. Baumann, W. Paul, T. Choi, C. P. Lutz, A. Ardavan, A. J. Heinrich, Electron paramagnetic resonance of individual atoms on a surface. *Science* **350**, 417–420 (2015).

44. W. Paul, S. Baumann, C. P. Lutz, A. J. Heinrich, Generation of constant-amplitude radio-frequency sweeps at a tunnel junction for spin resonance STM. *Rev. Sci. Instrum.* **87**, 074703 (2016).

45. S. Baumann, F. Donati, S. Stepanow, S. Rusponi, W. Paul, S. Gangopadhyay, I. G. Rau, G. E. Pacchioni, L. Gragnaniello, M. Pivetta, J. Dreiser, C. Piamonteze, C. P. Lutz, R. M. Macfarlane, B. A. Jones, P. Gambardella, A. J. Heinrich, H. Brune, Origin of perpendicular magnetic anisotropy and large orbital moment in Fe atoms on MgO. *Phys. Rev. Lett.* **115**, 237202 (2015).

46. W. B. Mims, Phase memory in electron spin echoes, lattice relaxation effects in CaWO$_4$: Er, Ce, Mn. *Phys. Rev.* **168**, 370–389 (1968).

47. M. Pelliccione, B. A. Myers, L. M. A. Pascal, A. Das, A. C. B. Jayich, Two-dimensional nanoscale imaging of gadolinium spins via scanning probe relaxometry with a single spin in diamond. *Phys. Rev. Appl.* **2**, 054014 (2014).

48. D. Schmid-Lorch, T. Häberle, F. Reinhard, A. Zappe, M. Slota, L. Bogani, A. Finkler, J. Wrachtrup, Relaxometry and dephasing imaging of superparamagnetic magnetite nanoparticles using a single qubit. *Nano Lett.* **15**, 4942–4947 (2015).

49. J.-P. Tetienne, A. Lombard, D. A. Simpson, C. Ritchie, J. Lu, P. Mulvaney, L. C. Hollenberg, Scanning nanospin ensemble microscope for nanoscale magnetic and thermal imaging. *Nano Lett.* **16**, 326–333 (2016).

50. B. Bryant, R. Toskovic, A. Ferrón, J. L. Lado, A. Spinelli, J. Fernández-Rossier, A. F. Otte, Controlled complete suppression of single-atom inelastic spin and orbital cotunneling. *Nano Lett.* **15**, 6542–6546 (2015).

51. T. Nozaki, Y. Shiota, S. Miwa, S. Murakami, F. Bonell, S. Ishibashi, H. Kubota, K. Yakushiji, T. Saruya, A. Fukushima, S. Yuasa, T. Shinjo, Y. Suzuki, Electric-field-induced ferromagnetic resonance excitation in an ultrathin ferromagnetic metal layer. *Nat. Phys.* **8**, 491–496 (2012).

Citation: P. Willke, W. Paul, F. D. Natterer, K. Yang, Y. Bae, T. Choi, J. Fernández-Rossier, A. J. Heinrich, C. P. Lutz, Probing quantum coherence in single-atom electron spin resonance. *Sci. Adv.* **4**, eaaq1543 (2018).

Science Advances

Probing quantum coherence in single-atom electron spin resonance

Philip Willke, William Paul, Fabian D. Natterer, Kai Yang, Yujeong Bae, Taeyoung Choi, Joaquin Fernández-Rossier, Andreas J. Heinrich and Christoper P. Lutz

ARTICLE TOOLS	http://advances.sciencemag.org/content/4/2/eaaq1543
SUPPLEMENTARY MATERIALS	http://advances.sciencemag.org/content/suppl/2018/02/12/4.2.eaaq1543.DC1
REFERENCES	This article cites 50 articles, 11 of which you can access for free http://advances.sciencemag.org/content/4/2/eaaq1543#BIBL
PERMISSIONS	http://www.sciencemag.org/help/reprints-and-permissions

Use of this article is subject to the Terms of Service